



HAL
open science

Defect-Rich Graphdiyne Quantum Dots as Efficient Electron-Donors for Hydrogen Generation

Wahid Ullah, Amine Slassi, Cong Wang, Erwan Paineau, Minh-Huong Ha-Thi, Thomas Pino, Zakaria Halime, Audrey Gayral, Maxime Vallet, Jéril Degrouard, et al.

► **To cite this version:**

Wahid Ullah, Amine Slassi, Cong Wang, Erwan Paineau, Minh-Huong Ha-Thi, et al.. Defect-Rich Graphdiyne Quantum Dots as Efficient Electron-Donors for Hydrogen Generation. *Advanced Energy Materials*, 2024, 14 (30), pp.2401547. 10.1002/aenm.202401547 . hal-04731743

HAL Id: hal-04731743

<https://hal.science/hal-04731743v1>

Submitted on 11 Oct 2024

HAL is a multi-disciplinary open access archive for the deposit and dissemination of scientific research documents, whether they are published or not. The documents may come from teaching and research institutions in France or abroad, or from public or private research centers.

L'archive ouverte pluridisciplinaire **HAL**, est destinée au dépôt et à la diffusion de documents scientifiques de niveau recherche, publiés ou non, émanant des établissements d'enseignement et de recherche français ou étrangers, des laboratoires publics ou privés.

Defect-Rich Graphdiyne Quantum Dots as Efficient Electron-Donors for Hydrogen Generation

*Wahid Ullah, Amine Slassi, Cong Wang, Erwan Paineau, Minh-Huong Ha-Thi, Thomas Pino, Zakaria Halime, Audrey Gayral, Maxime Vallet, Jéril Degrouard, Jérôme Cornil, Mohamed Nawfal Ghazzal**

Wahid Ullah, Cong Wang, Audrey Gayral, Mohamed Nawfal Ghazzal
Université Paris-Saclay, UMR8000 CNRS, Institut de Chimie Physique, 91405 Orsay, France
E-mail: mohamed-nawfal.ghazzal@universite-paris-saclay.fr

Amine Slassi
Cadi Ayyad University, ENS, Department of Physics, Marrakech, Morocco

Erwan paineau, Jéril Degrouard
Université Paris-Saclay, CNRS 8502 Laboratoire de Physique des Solides, 91405 Orsay, France

Minh-Huong Ha-Thi, Thomas Pino,
Université Paris-Saclay, CNRS Institut des Sciences Moléculaires d'Orsay, 91405 Orsay, France

Zakaria Halime
Université Paris-Saclay, CNRS UMR 8182 Institut de Chimie Moléculaire et des Matériaux d'Orsay, 91405 Orsay, France

Jérôme Cornil, Amine Slassi
Laboratory for Chemistry of Novel Materials, University of Mons, Place du Parc 20, Mons, 7000 Belgium

Maxime Vallet
Université Paris-Saclay, Laboratoire de Mécanique, CentraleSupélec, ENS Paris-Saclay, 91190, Gif-sur-Yvette, France

Keywords: graphdiyne, quantum dots, defects, electron donor, photocatalysis

Downsizing the graphdiyne's (GDY) network to shape quantum dots (QDs) would provide attractive optical and electronic properties associated with quantum confinement and edge effects. Here, we demonstrate that quantum confinement and defect introduction allow using GDY in donor-acceptor photocatalytic systems for solar-to-hydrogen conversion. The defect-rich GDY QDs (GDYO-QDs) exhibit a blue-to-green excitation-dependent photoluminescence

behavior, demonstrating their ability to harvest light over a wide energy range. Quantum-chemical calculations evidenced the increase of the electronic bandgap of GDY after quantum confinement and defect introduction without the appearance of trap states that could hamper charge transport properties. Such unique optical behavior of QDs was used in photocatalytic hydrogen generation through the hybridization with a TiO₂ surface as a model photocatalyst. Theoretical and experimental results demonstrate that the donor–acceptor system tremendously boosts the photocatalytic performance, reaching 5288 $\mu\text{mol g}^{-1}$ after 4 h of illumination at a constant rate of 1322 $\text{mol g}^{-1} \text{h}^{-1}$, using a low volume of sacrificial electron donor. The QDs act as efficient chromophores harvesting UV and visible light while injecting electrons into the TiO₂. This work opens a new area of using GDYO-QDs as an efficient chromophore in developing donor-acceptor systems for photocatalysis and future photovoltaic devices.

1. Introduction

Graphdiyne (GDY) is an emerging two-dimensional (2D) carbon allotrope consisting of alternated hybridized orbitals (sp and sp^2) arranged in a highly ordered honeycomb lattice structure that is predicted to exhibit unique electronic properties.^[1–3] The structure provides GDY with a highly rich π -conjugated scaffold, uniform pores distribution, high surface area, and high carrier mobility, enabling efficient charge transport, which can be utilized for various catalytic processes.^[4,5] Unlike graphene, a zero-bandgap material, the presence of carbon-carbon triple bonds introduces a bandgap in the electronic structure, allowing it to have semiconductor behavior and a tunable bandgap.^[6] While GDY was mainly used as a support for electrocatalytic or catalytic reactions,^[7,8] the opportunity to tune the bandgap has extended its use in energy applications. The heteroatoms doping, covalent and non-covalent molecular functionalization allowed tailoring of the electronic properties and increasing the active sites.^[9–20] A bottom-up method, aiming at H-substitution of the diacetylenic groups in the ortho and para position of the benzene rings of the conjugated network, has been proposed to open the GDY's bandgap and reach optimal interfacial charge separation and photocatalytic H₂ generation.^[21] The H-graphdiyne has also been demonstrated to be promising as an electrode material for hydrogen and oxygen evolution reactions.^[22–24] Despite the huge efforts made at exploring GDY as an attractive platform possessing tunable electronic properties, several challenges associated with GDY-size dependent properties are still to be addressed.^[25,26] The morphology, size, thickness, and number of layers of 2D nanosheets greatly influence their physical and chemical properties. Thus, downsizing a 2D carbon-based network to a finite size below 100 nm to shape QDs provides attractive optical and electronic properties associated

with quantum confinement and edge effects.^[27] In particular, the QDs exhibit a size-dependent bandgap behavior and higher absorption capability over wider spectral regions,^[28] which is strongly desirable in solar energy applications. Carbon based-QDs can be used to fabricate solar cells or interfaced as photosensitizers with metal oxides, giving rise to visible-light photocatalytic and photovoltaic devices.^[29] On this side, graphdiyne is yet to be fully explored to adopt structural rescaling and quantum confinement methods. Indeed, quantum confined materials could exhibit highly demanded optical properties and even generate hot electrons and holes that are key species in efficient photoredox reactions. To the best of our knowledge, graphdiyne quantum dots with tunable optical properties were mainly reported for their photoluminescent properties in biological detection.^[30,31]

In this work, we report the effect of quantum confinement of GDY with narrow size distribution on their optical, electronic, and photocatalytic properties. The GDYO-QDs were obtained using oxidative method, allowing the introduction of defects (functional groups) that provide the GDYO-QDs the ability to absorb solar light in a wide spectral range. Indeed, QDs exhibit an excitation-dependent PL behavior, shifting from blue to yellow as the excitation wavelength changes. The photoluminescence response translates the generation of discrete electronic levels. The GDYO-QD with extended π -electron systems was hybridized with a TiO₂ surface as a photocatalyst model to construct a donor-acceptor system and demonstrate the use of GDYO-QDs as electron donor (chromophore) for photocatalytic H₂ generation. Quantum confinement is expected to increase the electronic coupling between GDYO-QDs and TiO₂. At optimal loading, the GDYO-QDs/TiO₂ photocatalyst exhibited excellent donor-acceptor ability, where QDs were able to improve the photosensitization by increasing the light-harvesting capability and boosting the photocatalytic performance, using a low amount of sacrificial electron donor. The photocatalytic H₂ production was 23 times higher than pristine TiO₂. This work demonstrates using GDYO-QDs as an efficient chromophore and electron donor for photocatalytic H₂ generation.

2. Results and Discussion

The synthesis of GDYO-QDs is achieved by a top-down two-step process, which starts by cutting the pre-synthesized pristine GDY films, as shown in **Figure 1a**. The morphology changes occurring during the two-step process were analyzed by transmission electron microscopy (TEM) and reported in **Figures 1, S1, and S2**. The GDY, previously grown and peeled off from the Cu substrate, was oxidized in an acidic mixture of H₂O₂/H₂SO₄. The GDY and defect-rich GDY exhibit 2D sheet morphology, yet the layers in the GDY film are more

compact than GDYO (**Figure S1e-f** in supporting information). Essentially, the oxidation process exfoliates the GDY to a few transparent layer sheets with crinkles and folds visible in **Figure S1e, f**. The lattice spacing of 0.41 nm is visualized in the GDY sample after exfoliation and defects formation (**Figure S1h**). Then, the size of the GDYO film was further reduced using sonication for 1 h, followed by hydrothermal treatment (more details are reported in the supporting information). The hydrothermal treatment allows cutting GDYO and forming GDYO-QDs with a 5-6 nm diameter and atomic spacing of 0.38 nm, as shown in the high-resolution TEM **Figure 1 a-f** and **Figure S2**. The size of QDs and the atomic arrangement are in agreement with previous studies.^[30] The as-prepared GDYO-QDs are highly stable in solution, and no precipitation was observed over days of aging.

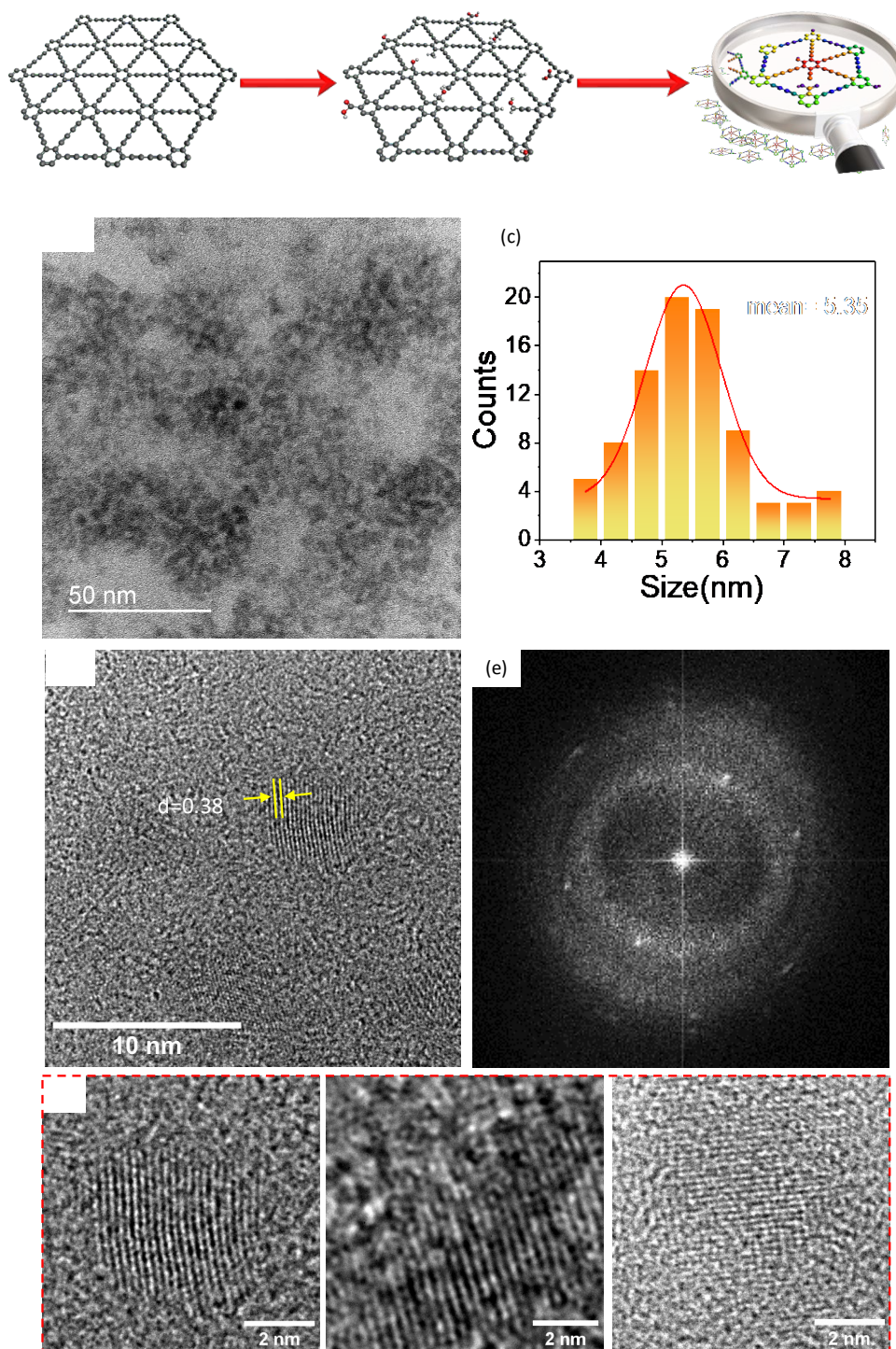


Figure 1. a) Schematic illustration of the experimental part for the GDYO-QDs fabrication. b, c) TEM image of GDYO-QDs and the corresponding size distribution. d, e) HR-TEM images of QDs with atomic arrangement and their Fast-Fourier-transform (FFT). f) HR-TEM images showing single QDs.

The bonding structure of GDY-based materials was characterized by Raman spectroscopy, and the results are shown in **Figure 2a**. The Raman spectroscopy revealed four bands typical of pristine GDY, which are D (1385.5 cm^{-1}), G (1566.7 cm^{-1}) bands of sp^2 bonded carbon atoms of aromatic rings, and two vibrations of the sp hybridized carbons of the diacetylenic group centered at 1934 and 2182.8 cm^{-1} . The relatively low ratio of $I_{\text{D}}/I_{\text{G}}$ (0.81) points towards fewer defects and a high degree of structural organization of the GDY.^[1] The successive oxidation, exfoliation, and hydrothermal treatment leading to the synthesis of GDYO-QDs also display D and G bands at 1385.5 cm^{-1} and 1566.6 cm^{-1} (green curve in **Figure 2a**), yet with higher $I_{\text{D}}/I_{\text{G}}$ ratio (~ 1), indicating an increase of defects into the structure. The peaks associated with sp hybridized carbons significantly decrease, suggesting preferential oxidation on the acetylenic bonds. Additionally, a higher background originating from strong fluorescence activity of the QDs over a wide spectral region during the Raman spectra acquisition overlapped with the signal of the acetylenic group, thus suppressing the Raman signals.^[32] The chemical structures and the appearance of polar functionalities in the QDs were also confirmed by Fourier Transform Infrared (FTIR) spectroscopy (**Figure S3**). The peaks at 1426 , 1593 , 1717 , 2920 , and 3415 cm^{-1} are assigned respectively to C–OOH, C=C, C=O, C–H, and O–H functions. Nevertheless, compared to GDY, the oxide and QDs samples exhibited supplementary and intense bands associated with bonded oxygen, indicating the successful chemical oxidation of the GDY surface and in agreement with previous studies.^[33] X-ray photoelectron spectroscopy (XPS) was used to investigate the chemical surface composition of GDY and GDYO-QD. The high-resolution C 1s spectra of GDY (**Figure S4**) are deconvoluted into four sub-peaks assigned to C=C (284.55 eV), C \equiv C (285.3 eV), C–O (286.6 eV) and C=O (288.2 eV). The ratio of sp/sp^2 carbon peaks is approximately 2, pointing to a high degree of structural organization and interconnection of benzene rings through the acetylenic linkages.^[34] The oxidation of GDY induces a chemical shift of the peak at 285 eV , and the appearance of a shoulder centered at 289 eV (**Figure 2b**) is assigned to the generation of O=C–O functional groups. Notably, the ratio of the peaks area of sp/sp^2 bonded carbon decreased upon oxidation. The weakening of the sp -carbon signal indicates a preferential breaking down of acetylenic groups compared to benzene rings during oxidation.

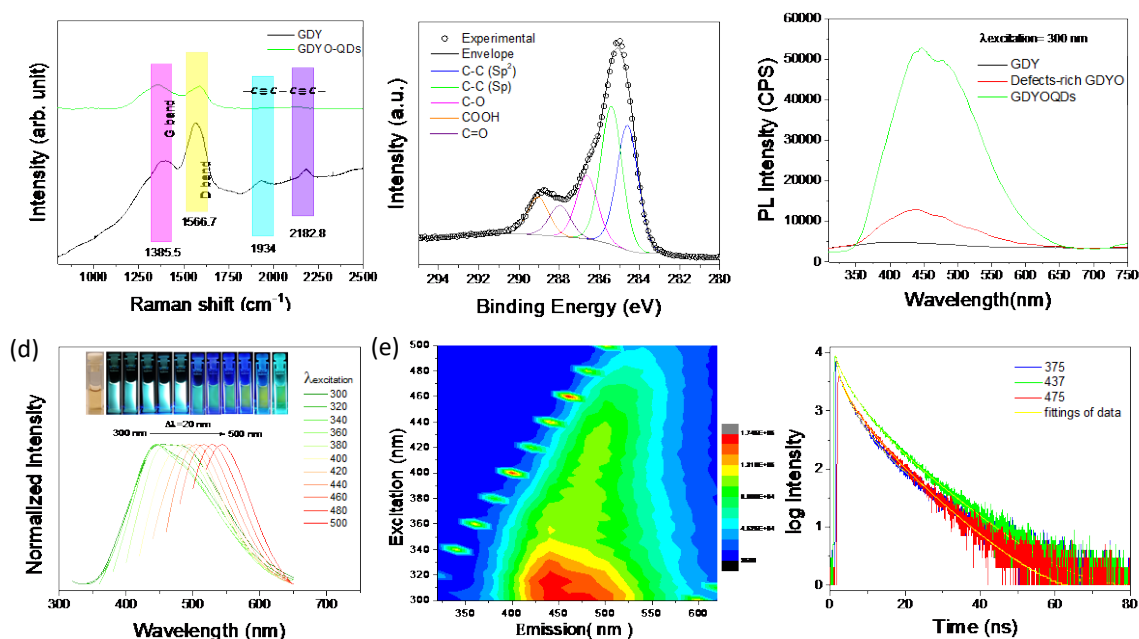


Figure 2. Structural and optical characterization. a) Raman analysis of GDY and GDYO-QDs, b) high resolution C 1s X-ray photoelectron spectroscopy (XPS) data of GDYO-QDs, c) comparison of photoluminescence (PL) spectra of GDY, GDYO and GDYO-QDs d) excitation dependent PL spectra of GDYO-QDs and image visualization of the fluorescence at the corresponding wavelengths shown in the inset, e) emission-excitation intensity 3D mapping and f) TR-PL fitted decay curves of GDYO-QDs, recorded at three different λ_{ex} .

The optical properties of the as-synthesized GDYO-QDs were evaluated using UV-vis and photoluminescence spectroscopies. The QDs showed a shifted absorbance to higher energy, compared to GDY and defects-rich GDY (supporting information **Figure S5**). Even though the QDs showed a broad absorption in the UV-visible spectral region, they left behind a tail-like decay in the near infra-red region. This originates from the electronic transitions between π - π^* and n - π^* of C=C and C≡C, and C=O bonded atoms of the GDYO-QDs skeleton. The photophysical processes in QD materials need comprehensive insight and detailed understanding. In defective QDs, surface states play a significant role not only in charge carriers' dynamics but also in influencing the fluorescence properties, for example, photoluminescence (PL) quenching and enhancement and inter and intra-molecular charge transfer mechanisms.^[35] Detailed PL analyses were conducted to gain a better insight into the quantum confinement and surface state defects of GDY-QDs. PL response of the GDYO-QDs exhibits very high photoemission compared to GDY and GDYO with a broad emission peak, shifting 50 nm away from the GDY peak, as shown in **Figure 2c**. The changes in the optical

response and peak shifting upon material hammering are attributed to the chemical modification of the GDY skeleton by oxy-functional groups, size rescaling, and layer exfoliation. We further explored the effect of the formation of these functional groups (defects) on the optical properties of GDYO-QDs by recording the PL emission spectra at various excitation wavelengths (λ_{ex}) ca. 300-500 nm (**Figure 2d**). Initially, by varying the λ_{ex} from 300 to 360 nm, the emission peak remains unchanged and centered at 460 nm. However, monitoring the λ_{ex} in the 380-500 nm range leads to a gradual red shift of the PL emission peak. Nevertheless, the intensity of peak maxima also decreases, which could reveal faster non-radiative recombination. The excitation-dependent optical behavior is further visualized in the recorded images (see inset of **Figure 2d**) at different wavelengths, displaying color variations from blue to green under monochromatic light following the trend of PL emission spectra. The fluorescence behavior is supported by 3D emission-excitation displayed in **Figure 2e**. The cartography allows the visualization of the relationship between excitation and emission, demonstrating that the QDs can be excited through a wide range of energy and yet show a large window of spectral emission with variable intensity. It is worth mentioning that some small islands are also visible on the left side of the main 3D mapping related to Rayleigh scattering due to high order scattering from the monochromator. The excitation-dependent fluorescence is attributed to the quantum confinement and the defects generated during the preparation of GDYO-QDs.^[36,37] We also conducted time-resolved photoluminescence (TR-PL) experiments, as shown in **Figure 2f**, to understand the recombination dynamics of GDYO-QDs by applying three different excitation wavelengths (375, 437, and 475 nm) while emission was adjusted according to the steady state PL from **Figure 2d**. The decay curves have almost the same intensity and are superimposed on each other. The data fitted well with triexponential decay functions, and the lifetime parameters are tabulated in supporting information (**Table S1**). The first decay τ_1 of GDYO-QDs is short and likely originates from the emission of intrinsic states of the GDY configuration. The relatively longer decay components (τ_2 and τ_3) are associated with various phenomena, including defects or functional groups (OH, COOH, and CO, etc.) on the surface of GDYO-QDs, quantum confinement effect, and surface traps.^[38] These results also support the FTIR (**Figure S3**) and XPS (**Figure 2b**) analysis, indicating the generation of functional groups on the QDs surface. This is also in agreement with PL emission spectra (**Figure 2d**) and photoluminescence excitation (PLE) results (**Figure S6**). The excited carriers were reported to be confined to the surface sites, making the surface defect fluorescence dominant so that increasing λ_{ex} yields a noticeable red shift.^[39] Similarly, the GDYO-QDs contain a mixture of

highly hybridized carbon (i.e., sp^3 , sp^2 , and sp) compared to other carbon materials, creating several surface states that can equally alter the PL properties of GDYO-QDs.

To further rationalize the experimental data, Density Functional Theory (DFT) calculations with periodic boundary conditions were carried out to evaluate the impact of the formation of oxygenated functional groups (OH, COOH, and COH) revealed by FTIR and XPS on the properties of the GDY and hybrid systems made with TiO_2 . First, we started our calculations by seeking the stable adsorption configurations of the oxygenated functional groups (OH, COOH, and COOH) on defective GDY with two/four carbon vacancies in the acetylene linkages that were shown experimentally to be the most affected upon oxidation; in the following, the results with two carbon vacancies will be presented in the core of the article while those obtained with four carbon vacancies will be collected in the supporting information. The most stable adsorption configurations retained for our study are shown in **Figure S7** (supporting information). It is found that the basal plane structure of the GDY layer is systematically preserved upon adsorption of the functional groups. The band structure computed for each system (**Figure 3 and S8**) revealed that the adsorption of such oxygenated functional groups on GDY significantly opens its band gap by 30%, from 0.69 eV (for GDY pristine) up to 1.01 eV (with functional groups). This is in full agreement with the blue shift of the absorption band of GDYO-QDs upon oxidation. Importantly, no trap states were observed within the bandgap, thus ensuring that the functionalization will not deeply affect the charge transport properties.

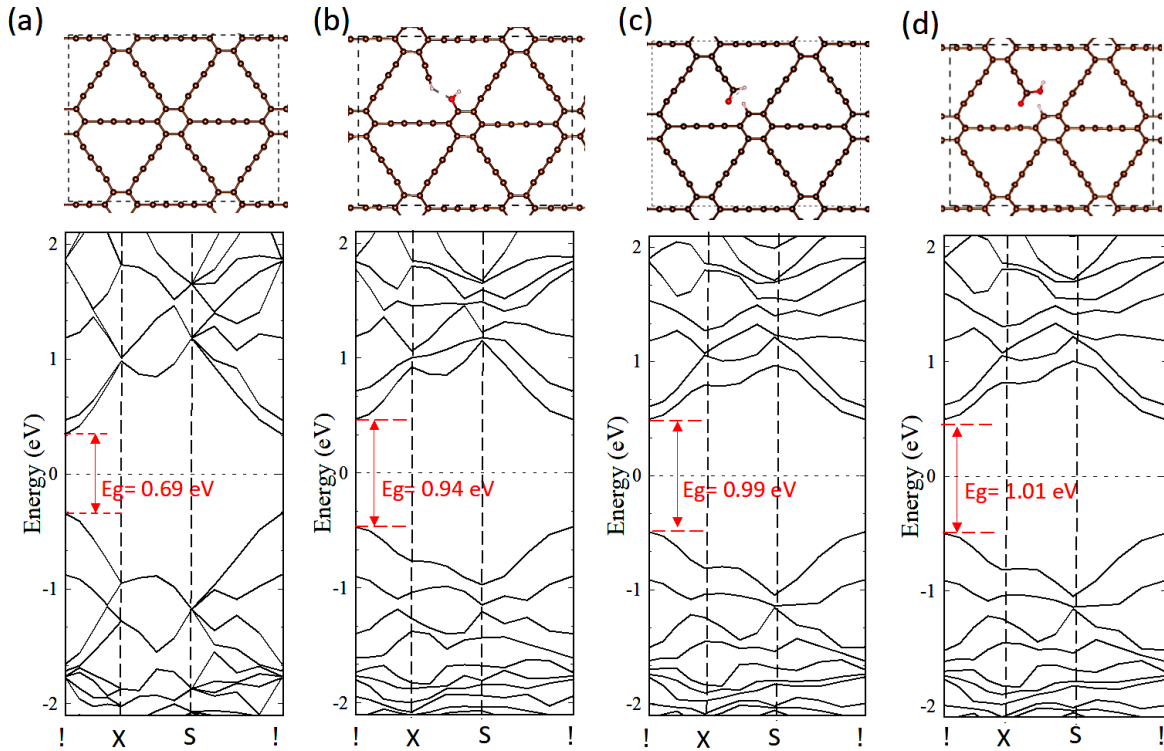


Figure 3. Top view of representative adsorption configurations of oxygenated functional groups and their band structures calculated at DFT/HSE level. The band structures of additional configurations are shown in Figure S8 in SI.

Next, we consider the heterostructure systems by placing GDY and its oxygenated counterparts on the main exposed (101) surface of TiO_2 , which is non-polar. The optimized structures of the built GDYO-QDs/ TiO_2 interfaces are shown in **Figure 4** and **Figure S9** in supporting information. Due to the large size of the systems, the binding energy was calculated at the DFT/PBE level by including van der Waals corrections using the following equation:

$$E_{int} = E_{tot} - E_{\text{TiO}_2} - E_{\text{GDY}} \quad (1)$$

where E_{tot} , E_{TiO_2} and E_{GDY} are the total energies of the heterostructure, TiO_2 layer and GDYO-QDs layers in the different configurations, respectively, in the geometry of the interacting relaxed heterostructures. The equilibrium geometries of the heterostructures are given in **Figure 4** and **Figure S9**. The GDY monolayer can undergo a non-negligible buckling at the interfaces due to Coulomb attraction or repulsion between the oxygenated functions and the underneath atoms in the TiO_2 surface. As a matter of fact, some oxygenated functional groups, such as COH and COOH, move away from the GDYO-QDs surface due to repulsive interaction with oxygen atoms of the TiO_2 surface (**Figure 4c, d**). On the other hand, in the case of OH substitution, the hydrogen atom is attracted by oxygen atoms of the TiO_2 surface (**Figure 4b**).

More importantly, the calculated binding energy values demonstrate that the adsorption of functional groups improves the adhesion energy of the heterostructure in each case, with the largest increase observed for the OH functionalization. The larger adhesion energy originates from a more pronounced charge transfer between TiO₂ and defective GDYs, thus yielding an extra Coulomb stabilization.

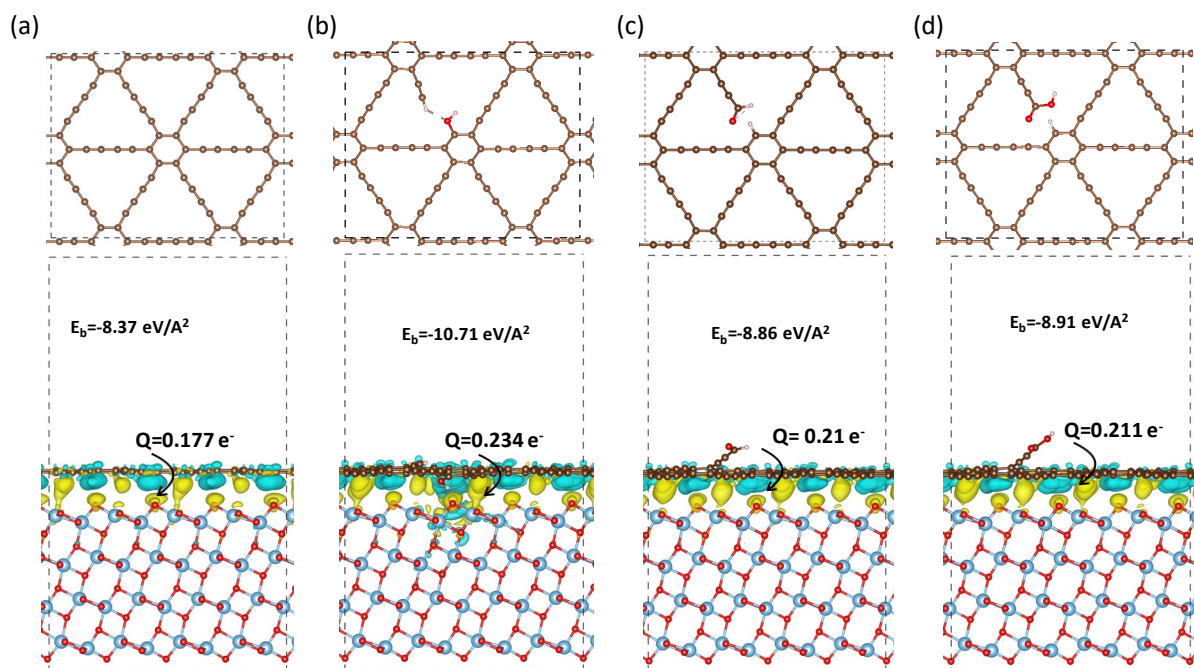


Figure 4. Equilibrium structure of the hybrid systems for a) pristine GDY and defective GDY with oxygenated functional groups: b) –OH, c) –COH, and d) –COOH

Owing to their exceptional optical properties and ability to act as electron donors (chromophores) revealed by the DFT calculations (*vide infra*), GDYO-QDs were evaluated for photocatalytic H₂ evolution reaction by making hybrids with TiO₂-P25. To do so, various weight % (1, 2, 3, 5, and 10 %) loading of QDs is hybridized with commercial TiO₂-P25 as model photocatalyst (experimental details are given in supporting information), and their photocatalytic efficiency is evaluated. The HR-TEM image in **Figure 5a** unveils the successful hybridization. The spherical QDs are attached to TiO₂ nanoparticles with 0.34 nm (101) lattice spacing (supporting information **Figure S10**). The Wide-Angle X-ray scattering (WAXS) analysis of the nanostructure exhibits a mixture of anatase and rutile crystalline phase, typical of P25, without any significant change after the formation of QDYO-QDs/TiO₂ interface (supporting information **Figure S11**). The high-resolution Ti 2p peaks centered at 459 and 464.7 eV, assigned to Ti 2p_{3/2} Ti 2p_{1/2}, respectively, with a satellite contribution at 472 eV (**Figure 5b**). It is obvious that with increasing GDYO-QDs contents loading, the peak

intensities gradually decrease. A slight positive shift at Ti 2p_{3/2} is also noticeable, attesting to the strong interaction with TiO₂, which is in agreement with DFT calculations. The high-resolution C 1s peak in **Figure 5c** presents identical contributions as previously observed for pure GDYO-QDs (**Figure 2b**), pointing to the preservation of GDYO-QDs skeleton after hybridization, also in agreement with TEM observations. Moreover, surface crystallinity, defects, and hybridization of the GDYO-QDs/TiO₂ were also elaborated by employing Raman vibrational spectroscopy (**Figure 5d**). Under the illumination of laser source at 532 nm, pure TiO₂ projected with several Raman bands ca. 138.4 cm⁻¹, 394.4 cm⁻¹, 514.2 cm⁻¹ and 636.8 cm⁻¹ respectively assigned to the E_{g(1)}, B_{1g(1)}, A_{1g} + B_{1g(2)}, and E_{g(3)} symmetries of TiO₂ anatase modes (**Figure 5d**). GDYO-QDs/TiO₂ hybrid samples also exhibit the typical anatase Raman vibration modes with two additional peaks at 1338.5 cm⁻¹ and 1567.3 cm⁻¹ corresponding to the D and G bands of GDYO-QDs; they become more prominent with increasing QDs concentration, thus confirming the hybridization between GDYO-QDs and TiO₂ nanoparticles. This confirms that the anatase phase of TiO₂ and the main structure of GDYO-QDs remains intact in the composites. Nevertheless, compared with the peaks of free TiO₂, the main peak E_{g(1)} in GDYO-QDs/TiO₂ hybrids is gradually red shifted from 138 cm⁻¹ to 143 cm⁻¹. Similarly, the A_{1g} + B_{1g(2)} modes are also projected with a slight shift from 514.2 cm⁻¹ to 508.6 cm⁻¹ with increasing QDs wt.%, as shown in the high magnification views of Raman curves in **Figure 5e, f**. These Raman bands reveal a strong interaction between GDYO-QDs and TiO₂ nanocrystals.^[40] A shift to lower wavenumber also suggests a weakening of the Ti-O bonds, which may be due to electron transfer from GDYO-QDs to TiO₂.^[41] It is worth mentioning that the noisy background and fringes in the Raman curves of hybrid samples are due to the interference of strong emission from the fluorescent GDYO-QDs. Similarly, FTIR spectra of the GDYO-QDs/TiO₂ displayed a strong band between 450-870 cm⁻¹ region associated with Ti-O-Ti/Ti-O-H stretching mode, consistent with Raman results, and the peaks around 1622 and 3400 cm⁻¹ are respectively the classical Ti-OH stretching and O-H vibration (**Figure S12a**). The GDYO-QDs/TiO₂ composites also exhibited extra peaks of the GDYO-QDs skeleton around 1200, 1380, and 1550 cm⁻¹ originating from the C-OH, C=O, and C=C vibration modes, respectively. The absorption band of TiO₂ is affected by interfacing GDYO-QDs, as shown by UV-visible spectra (**Figure S12b**). With the incorporation of GDYO-QDs, the absorption range is extended towards lower energy, and the absorption intensity gradually increases as the amount of QDs content increases.

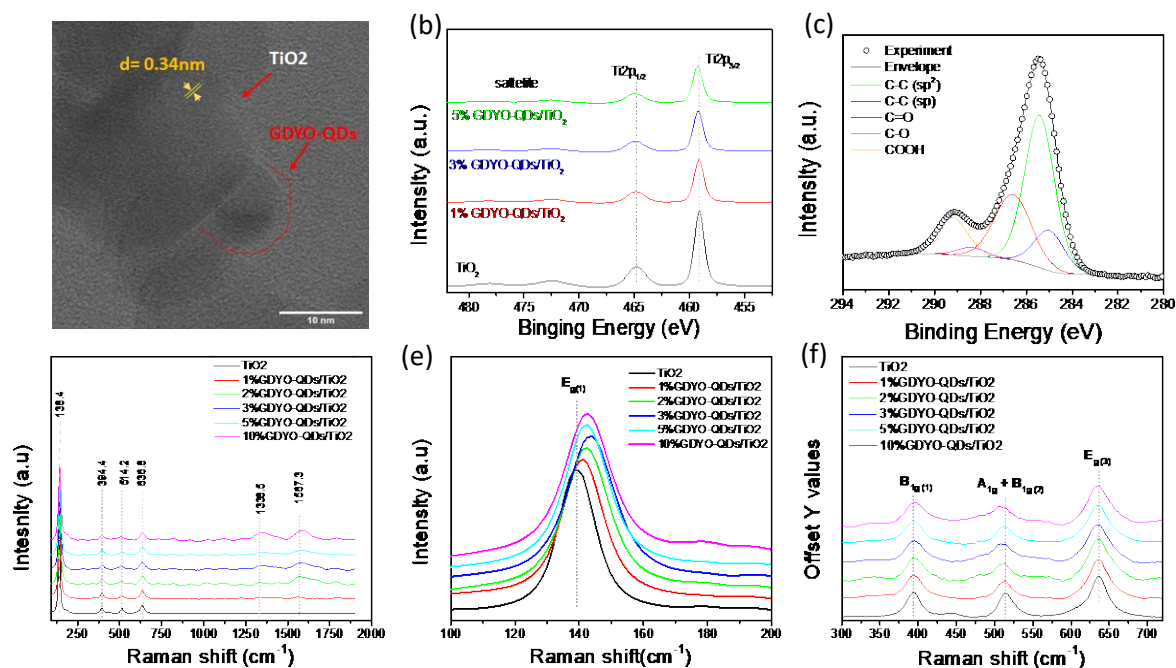


Figure 5. Morphological and structural characterization of GDYO-QDs/TiO₂ samples. a) HR-TEM, b, c) high-resolution Ti 2p and C 1s XPS spectra, respectively, d) Raman vibration of GDYO-QDs/TiO₂, and e, f) high magnification of characteristic Raman vibration modes

The photocatalytic hydrogen generation was performed under UV-visible and visible light (>400 nm) excitations in aqueous solutions containing 6% in volume of triethanolamine (TEOA) as a sacrificial electron donor (**Figure 6**). Interfacing GDYO-QDs with TiO₂ shows an impressive enhancement of the photocatalytic H₂ generation. The optimal weight ratio of the QDs was 1-2 wt.%. The hydrogen generation, which was very low for pristine TiO₂, reaches a total amount of $\sim 5288 \mu\text{mol g}^{-1}$ for 1 % GDYO-QDs/TiO₂ after 4 h of illumination (**Figure 6a**), corresponding to an average $\sim 1322 \mu\text{mol h}^{-1} \text{g}^{-1}$ H₂ production rate. The amount of H₂ remained unchanged up to 2 wt.% of QD loading, which indicates reaching a saturation level in terms of photocatalytic activity. Nonetheless, further elevation in GDYO-QDs concentration (ca. 3, 5, and 10 wt.%) has an inverse effect and gradually decreased the amount of H₂ generation to $2429 \mu\text{mol g}^{-1}$ for 10% GDYO-QDs/TiO₂ at an average rate of $607 \mu\text{mol h}^{-1} \text{g}^{-1}$ (**Figure 6b**), even though, the H₂ production remains much higher compared to nonmodified TiO₂. The results indicate that optimal coverage of the TiO₂ surface should reach up to 2 wt% while increasing the number of QDs at the surface beyond this threshold probably blocks active sites where the reduction reaction occurs, decreasing the H₂ production. The stability of the composite was also assessed through cycling experiments, and the results show only 17 % decrease after four consecutive cycles, indicating the hybrid material long-lasting stability and durability for the hydrogen evolution reaction (**Figure 6c**). Previously, we observed that GDYO-QDs are also

capable of harvesting visible light, predominantly attributed to the quantum confinement effect and surface defects in the materials and, therefore, of generating electrons that can be injected into the host TiO₂ surface. Under visible light illumination (**Figure 6d**), the QDs/TiO₂ hybrid samples exhibit significant photocatalytic activity for H₂ production compared to TiO₂-P25 alone. Indeed, P25 shows no activity under visible light, while an average rate of 132.7 μmol h⁻¹ g⁻¹ was obtained for 1 % GDYO-QDs/TiO₂. Moreover, the photocatalytic activity trend is similar to what has been observed under UV-vis light excitation. GDY and GDYO were hybridized with TiO₂ under an optimal ratio of 1wt%, and their activities were compared to GDYO-QDs. GDY and its oxidized form exhibited similar photocatalytic H₂ evolution, as shown in **Figure 6e**. Although the photocatalytic activity of TiO₂ improves, it remains far below the efficiency of 1% GDYO-QDs/TiO₂. The photocatalytic H₂ evolution performance of GDYO-QDs/TiO₂ is compared with previously reported GDY-based composites and listed in **Table S2**. The metals-free hybrid photocatalyst, which used only 1wt% of QDs and twice as low of a sacrificial electron donor, generated an impressive amount of H₂. These results demonstrated the role of GDYO-QDs in photosensitization and electron injection in the TiO₂ for H₂ generation.

To further investigate the hybrid photocatalyst's performance, we employed photoelectrochemistry to determine the light-dependent response by recording their transient photocurrent under monochromatic light excitation, λ_{ex} ca. 300-540 nm (**Figure S13**). Initially, by increasing the λ_{ex}, the photocurrent intensities were increased for all samples. TiO₂-P25 absorbs light in the ultraviolet region, and here, the maximum photocurrent for bare TiO₂ was reached at λ_{ex}=360 nm and started to reduce with further increment in λ_{ex}. Instead, our GDYO-QDs/TiO₂ exhibited higher photocurrent intensity and significant light absorption capability over a wider spectral region from UV to visible. However, note that the photocurrent, in the case of higher GDYO-QD (5% and 10 %) concentration, decreased again, similarly to what we observed during photocatalytic measurements. The single wavelength based photoelectrocatalytic behavior of GDYO-QDs exclusively follows the photocatalytic trends and highlights the role of GDYO-QDs in the light harvesting capability. The apparent quantum efficiency of 3.87 % is achieved for 1% GDYO-QDs/TiO₂, illuminating at 400 nm wavelength generated from a monochromator (calculation details are given in supporting information). Moreover, the charge separation and transfer efficiency of the GDYO-QDs/TiO₂ was also realized by recoding electrochemical impedance spectroscopy (EIS) under simulated solar light in the frequency range of 10⁵ – 0.1 Hz at open circuit potential. The EIS Nyquist plot, fitted with an equivalent circuit (inset), is shown in **Figure S14**, and the obtained data of the resistance

parameter is tabulated in **Table S3**. The semicircles radius of the Nyquist plot of all GDYO-QDs/TiO₂ hybrids are significantly smaller than that of pure TiO₂-P25, demonstrating that the hybrids experience lower charge transfer resistance, which facilitates the photogenerated charge carrier dynamics and electron-hole separations. The solution resistance (R_s) values did not significantly differ because the tests were performed in the same bulk electrolyte solution (**Table S3**).^[42] However, the charge transfer resistance (R_p) values rapidly decrease with 1% GDYO-QDs hybridization, pointing to the fast charge transfer process at the electrode surface.

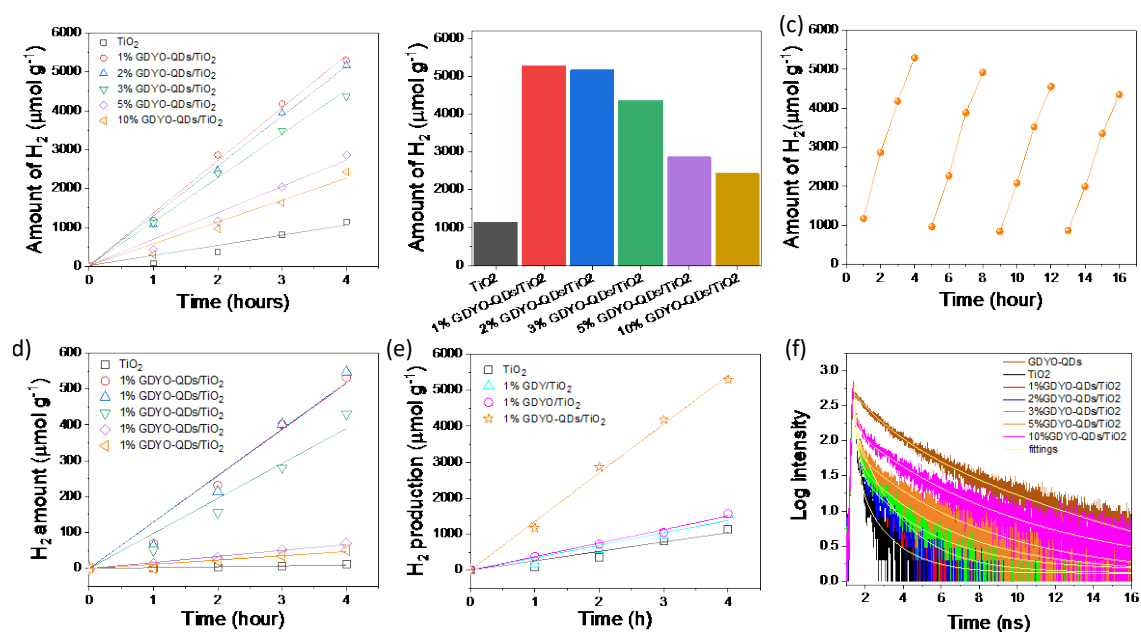


Figure 6. Photocatalytic hydrogen generation over commercial TiO₂-P25 and our fabricated GDYO-QDs/TiO₂ hybrid photocatalysts; a) time-coursed H₂ generation under the illumination UV-visible light over different photocatalysts using 6% (v/v) triethanolamine as sacrificial electron donor, b) comparison of the amount of H₂ produced, for different photocatalysts, after four hours irradiation, c) cyclic activity of 1%GDYO-QDs/TiO₂ photocatalyst for H₂ generation, d) time-coursed H₂ generation under visible light (>400 nm) over different photocatalysts, e) comparison of the photocatalytic H₂ generation with TiO₂-P25, 1% GDY/TiO₂, 1% defects-rich GDY/TiO₂ and 1% GDYO-QDs/TiO₂ hybrids f) time-resolved PL decays recorded at λ_{em} 430 nm using excitation source λ_{ex} 373 nm.

The substantial rise in photocatalytic performance matches the capability of GDYO-QDs to harvest a wide range of UV-visible light. To further understand the photocatalytic activity of GDYO-QDs/TiO₂ hybrids, the PL emission spectra were recorded for GDYO-QDs/TiO₂ and are shown in **Figure S15**. The samples exhibit peaks shifting by around 8 nm compared to TiO₂-P25, attributed to the interaction of QDs with the TiO₂ surface. The quantum confinement

of GDYO-QDs bears several oxygen functional groups that allow the QDs adhesion over the TiO₂ surfaces. This leads to the formation of GDYO-QDs/TiO₂ hybrids, which is in agreement with DFT calculations and the observed Raman shift. The emission signals were strongly quenched, ca. 35 %, in the presence of 1 wt.% GDYO-QDs and up to 50% with 10 wt. % QDs. This reflects the prolonged charge carrier lifetime in the GDYO-QDs/TiO₂ hybrids, pointing to the electron injection into the conduction band of TiO₂.

The electron injection mechanism from QDs to TiO₂ was assessed by titrating GDYO-QDs suspension against TiO₂ nanoparticles (aqueous dispersion). The PL behavior was recorded at 320 nm excitation wavelength, as shown in **Figure S16**. By adding TiO₂ aliquot, the PL emission intensities are gradually quenched with the increasing TiO₂ concentration, revealing the electron injection from GDYO-QDs to the TiO₂ photocatalyst, in agreement with TRPL results. For the validation of this argument and a detailed understanding of the carrier dynamics, we performed TRPL measurements of hybrids and the control samples (**Figure 6f**) at λ_{em} 430 nm and λ_{ex} 375 nm as source of energy. The curves were fitted with a tri-exponential decay function to obtain the decay parameters collected in **Table S4** in supporting information. Compared to GDYO-QDs, the delay time of free TiO₂ is very short, indicating the fast recombination of photogenerated electron-hole pairs. Contrary, GDYO-QDs/TiO₂ samples exhibit intermediate decay curves, and an increasing trend is observed in the decay time (compare the average lifetimes in **Table S4**) with a gradual increment of QDs wt.%, also in line with the steady-state PL results. We also recorded the TRPL curves of hybrids and control sample (**Figure S17**) with low energy excitation source ca. λ_{ex} 437 nm. The QDs/TiO₂ hybrid materials show significantly lower decay lifetime kinetics compared to QDs alone (**Table S5**). The results indicate that once the QDs harvest light over a wider range, the excited electrons are injected into the conduction band of TiO₂ before relaxing to the ground state, in agreement with steady-state PL. **Figure 7** depicts the computed band alignment at the interface between TiO₂ and all GDYO-QDs monolayers. The results show that the bottom of the conduction band is raised in all defective GDY compared to the pristine system, which should facilitate electron transfer to the conduction band of TiO₂, which is in agreement with the experimental results. Essentially, these QDs, with several surface functional groups, create defects, surface states, and a rich intrinsic π -conjugated configuration with the ability to capitalize the donor-acceptor chemistry to establish a synergy with the TiO₂ crystals. Based on the above results, we proved successful at tuning the electronic properties of GDY using quantum confinement effects and by generating defects such as functional groups at the surface. The GDYO-QDs possess the ideal electronic band structure to act as an efficient electron donor (chromophore) capable of

injecting electrons to the CB of TiO₂ and thus improving its photocatalytic efficiency for hydrogen evolution reaction. Following these investigations, we can establish that GDYO-QDs are able to harvest the UV-visible light and photosensitize TiO₂ for H₂ generation. Based on these results, we proposed that a synergy is being created between the components of the GDYO-QDs/TiO₂ hybrid under light irradiation and by generating and exchanging charge carrier flux. QDs harvest the light energy and generate excited electrons that are ultimately injected into the TiO₂ conduction band, allowing an efficient H⁺/H₂ conversion reaction, as proposed in the schematic illustration in **Figure S18**.

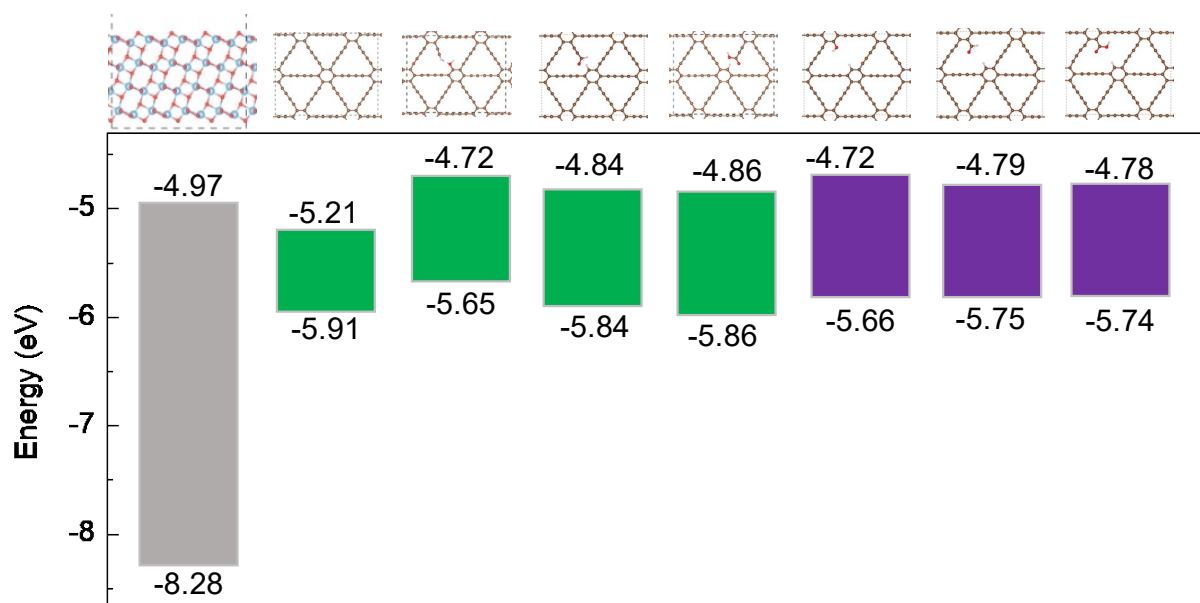


Figure 7. Band alignment of the isolated components calculated at the DFT/HSE level. The energy values are defined with respect to the vacuum level.

3. Conclusion

To summarize, GDY is hammered by chemical oxidation and hydrothermal treatment to fabricate defect-rich GDY-QDs of around 10 nm diameter, which bear several oxygen functional groups and display long-term stability and high solubility in water. The spectroscopic and microscopic methods employed in this study reveal the GDY surface functionalization and rescaling into QDs while retaining the main GDY structure. Compared to pristine GDY, the defects-rich GDY-QDs displayed excitation-dependent photoluminescence from UV to visible range. Quantum-chemical calculations further support the interpretation of the experimental

results. The introduction of oxygen functionality is also found to increase the band gap. We hybridized the QDs with commercial TiO₂-P25 nanoparticles at moderate conditions to form a model GDYO-QDs/TiO₂ hybrid photocatalytic regime. TEM, XPS, UV-visible, Raman, and FTIR and theoretical calculation provided important information on GDYO-QDs loading and surface interaction with TiO₂ nanoparticles. Steady-state PL and TRPL results reveal the electron injection from QDs to TiO₂. The GDYO-QDs/TiO₂ hybrid exhibited promising photocatalytic hydrogen generation in aqueous solution under UV-visible and visible light excitation. We reported 1322 $\mu\text{mol g}^{-1} \text{h}^{-1}$ of hydrogen production with 1%GDYO-QDs/TiO₂ hybrid sample under UV-visible. The weight percent amount of GDYO-QDs in the composite is crucial for the photocatalytic activity. The higher amount of hydrogen production was obtained using only 1 wt.% of GDYO-QDs. The visible light harvesting capability of GDYO-QDs allows extending the activity in the visible range, reaching a production H₂ rate of 132 $\mu\text{mol g}^{-1} \text{h}^{-1}$. This work opens a new area of using GDYO-QDs as an efficient chromophore, and its use could be extended in developing future photovoltaic devices.

4. Experimental Section/Methods

The experimental details of GDY materials synthesis, characterization, and their computational details are listed in the supporting information.

Supporting Information

Supporting Information is available from the Wiley Online Library or from the author.

Acknowledgments

The French National Research Agency (ANR) supported the work through the IngenCat project (ANR-20-CE43-0014). MNG acknowledges the ACT program (Accelerating CCS Technologies, Horizon2020 Project No. 691712) and the French National Research Agency (ANR) for the financial support of the NEXTCCUS project (project ID: 327327). MNG and WU acknowledge the Institute National de Chimie (INC) and CNRS for the financial support through the EMERGENCE@2023 program. The work in Mons is supported by the Belgian National Fund for Scientific Research (FRS-FNRS). Computational resources were provided by the Consortium des Équipements de Calcul Intensif (CÉCI), funded by F.R.S.-FNRS under Grant 2.5020.11. J.C. is an FNRS research director. MNG is grateful to Jean-Sébastien Lauret for the scientific discussion and to Diana Dragoë for performing the XPS analysis.

Received: ((will be filled in by the editorial staff))

Revised: ((will be filled in by the editorial staff))

Published online: ((will be filled in by the editorial staff))

References

- [1] G. Li, Y. Li, H. Liu, Y. Guo, Y. Li, D. Zhu, *Chemical Communications* **2010**, *46*, 3256.
- [2] D. Malko, C. Neiss, A. Görling, *Physical Review B* **2012**, *86*, 045443.
- [3] J. Li, X. Gao, L. Zhu, M. N. Ghazzal, J. Zhang, C.-H. Tung, L.-Z. Wu, *Energy & Environmental Science* **2020**, *13*, 1326.
- [4] C. Huang, Y. Li, N. Wang, Y. Xue, Z. Zuo, H. Liu, Y. Li, *Chemical Reviews* **2018**, *118*, 7744.
- [5] B. Li, C. Lai, M. Zhang, G. Zeng, S. Liu, D. Huang, L. Qin, X. Liu, H. Yi, F. Xu, N. An, L. Chen, *Advanced Energy Materials* **2020**, *10*, 2000177.
- [6] D. Malko, C. Neiss, F. Viñes, A. Görling, *Physical Review Letters* **2012**, *108*, 086804.
- [7] I. Muhammad, S. Ahmed, H. Cao, Z. Yao, D. Khan, A. Mahmood, T. Hussain, X.-G. Xiong, R. Ahuja, Y.-G. Wang, *Materials Today Chemistry* **2023**, *34*, 101756.
- [8] X. Gao, H. Liu, D. Wang, J. Zhang, *Chemical Society Reviews* **2019**, *48*, 908.
- [9] X. Zheng, X. Gao, R. A. Vilá, Y. Jiang, J. Wang, R. Xu, R. Zhang, X. Xiao, P. Zhang, L. C. Greenburg, Y. Yang, H. L. Xin, X. Zheng, Y. Cui, *Nature Nanotechnology* **2023**, *18*, 153.
- [10] M. Cui, P. Xin, Z. Che, M. Zou, M. Zhang, X. Sun, Y. Yuan, Z. Zou, G. Lv, S. Wang, W. Hu, *Chemical Engineering Journal* **2023**, *464*, 142629.
- [11] S. Chandra Shekar, R. S. Swathi, *Carbon* **2018**, *126*, 489.
- [12] Z. Zhu, Q. Bai, S. Li, S. Li, M. Liu, F. Du, N. Sui, W. W. Yu, *Small* **2020**, *16*, 2001440.
- [13] B. Liu, S. Zhan, J. Du, X. Yang, Y. Zhao, L. Li, J. Wan, Z.-J. Zhao, J. Gong, N. Yang, R. Yu, D. Wang, *Advanced Materials* **2023**, *35*, 2206450.
- [14] H. Bu, M. Zhao, H. Zhang, X. Wang, Y. Xi, Z. Wang, *The Journal of Physical Chemistry A* **2012**, *116*, 3934.
- [15] Y. Zhao, J. Wan, H. Yao, L. Zhang, K. Lin, L. Wang, N. Yang, D. Liu, L. Song, J. Zhu, L. Gu, L. Liu, H. Zhao, Y. Li, D. Wang, *Nature Chemistry* **2018**, *10*, 924.
- [16] F. Wang, Z. Zuo, L. Li, K. Li, F. He, Z. Jiang, Y. Li, *Angewandte Chemie International Edition* **2019**, *58*, 15010.

- [17] J. Xu, Q. Wan, M. Anpo, S. Lin, *The Journal of Physical Chemistry C* **2020**, *124*, 6624.
- [18] J. He, N. Wang, Z. Yang, X. Shen, K. Wang, C. Huang, Y. Yi, Z. Tu, Y. Li, *Energy & Environmental Science* **2018**, *11*, 2893.
- [19] C. Xie, X. Hu, Z. Guan, X. Li, F. Zhao, Y. Song, Y. Li, X. Li, N. Wang, C. Huang, *Angewandte Chemie International Edition* **2020**, *59*, 13542.
- [20] T. Lu, J. He, R. Li, K. Wang, Z. Yang, X. Shen, Y. Li, J. Xiao, C. Huang, *Energy Storage Materials* **2020**, *29*, 131.
- [21] J. Li, A. Slassi, X. Han, D. Cornil, M. Ha-Thi, T. Pino, D. P. Debecker, C. Colbeau-Justin, J. Arbiol, J. Cornil, M. N. Ghazzal, *Advanced Functional Materials* **2021**, *31*, 2100994.
- [22] T. Zhang, Y. Hou, V. Dzhagan, Z. Liao, G. Chai, M. Löffler, D. Olianias, A. Milani, S. Xu, M. Tommasini, D. R. T. Zahn, Z. Zheng, E. Zschech, R. Jordan, X. Feng, *Nature Communications* **2018**, *9*, 1140.
- [23] X. Zhou, B. Fu, L. Li, Z. Tian, X. Xu, Z. Wu, J. Yang, Z. Zhang, *Nature Communications* **2022**, *13*, 5770.
- [24] Y. Guo, J. Liu, Q. Yang, L. Ma, Y. Zhao, Z. Huang, X. Li, B. Dong, X.-Z. Fu, C. Zhi, *Small* **2020**, *16*, 1907341.
- [25] J. Li, X. Han, D. Wang, L. Zhu, M. Ha-Thi, T. Pino, J. Arbiol, L. Wu, M. Nawfal Ghazzal, *Angewandte Chemie* **2022**, *134*, e202210242.
- [26] M. Wang, J. Pu, Y. Hu, Y. Zi, Z.-G. Wu, W. Huang, *Advanced Functional Materials* **2024**, *34*, 2308601.
- [27] M. Bacon, S. J. Bradley, T. Nann, *Particle & Particle Systems Characterization* **2014**, *31*, 415.
- [28] S. Zhuo, M. Shao, S.-T. Lee, *ACS Nano* **2012**, *6*, 1059.
- [29] J. N. Tiwari, A. N. Singh, S. Sultan, K. S. Kim, *Advanced Energy Materials* **2020**, *10*, 2000280.
- [30] H. Min, Y. Qi, Y. Chen, Y. Zhang, X. Han, Y. Xu, Y. Liu, J. Hu, H. Liu, Y. Li, G. Nie, *ACS Applied Materials & Interfaces* **2019**, *11*, 32798.
- [31] J. Guo, M. Guo, F. Wang, W. Jin, C. Chen, H. Liu, Y. Li, *Angewandte Chemie International Edition* **2020**, *59*, 16712.
- [32] M. T. Gebrekidan, C. Knipfer, F. Stelzle, J. Popp, S. Will, A. Braeuer, *Journal of Raman Spectroscopy* **2016**, *47*, 198.
- [33] H. Yan, S. Guo, F. Wu, P. Yu, H. Liu, Y. Li, L. Mao, *Angewandte Chemie*

International Edition **2018**, *57*, 3922.

- [34] R. Matsuoka, R. Sakamoto, K. Hoshiko, S. Sasaki, H. Masunaga, K. Nagashio, H. Nishihara, *Journal of the American Chemical Society* **2017**, *139*, 3145.
- [35] D. Sebastian, A. Pallikkara, H. Bhatt, H. N. Ghosh, K. Ramakrishnan, *The Journal of Physical Chemistry C* **2022**, *126*, 11182.
- [36] J. Peng, W. Gao, B. K. Gupta, Z. Liu, R. Romero-Aburto, L. Ge, L. Song, L. B. Alemany, X. Zhan, G. Gao, S. A. Vithayathil, B. A. Kaiparettu, A. A. Marti, T. Hayashi, J.-J. Zhu, P. M. Ajayan, *Nano Letters* **2012**, *12*, 844.
- [37] H. Kalita, J. Mohapatra, L. Pradhan, A. Mitra, D. Bahadur, M. Aslam, *RSC Advances* **2016**, *6*, 23518.
- [38] Z. Gan, H. Xu, Y. Hao, *Nanoscale* **2016**, *8*, 7794.
- [39] X. Wen, P. Yu, Y.-R. Toh, X. Hao, J. Tang, *Advanced Optical Materials* **2013**, *1*, 173.
- [40] G. Peng, J. E. Ellis, G. Xu, X. Xu, A. Star, *ACS Applied Materials & Interfaces* **2016**, *8*, 7403.
- [41] Z. Li, R. Ye, R. Feng, Y. Kang, X. Zhu, J. M. Tour, Z. Fang, *Advanced Materials* **2015**, *27*, 5235.
- [42] G. Cai, Z. Yu, R. Ren, D. Tang, *ACS Sensors* **2018**, *3*, 632.